




Acid-base properties of hydroxyapatite(0001) by the adsorption of probe molecules: An *ab initio* investigation

Albert F. B. Bittencourt ¹, Paulo C. D. Mendes ², Gustavo P. Valença ¹ and Juarez L. F. Da Silva ^{2,*}

¹School of Chemical Engineering, University of Campinas, 13083-852 Campinas, SP, Brazil

²São Carlos Institute of Chemistry, University of São Paulo, P.O. Box 780, 13560-970 São Carlos, SP, Brazil



(Received 19 January 2021; revised 12 May 2021; accepted 2 July 2021; published 26 July 2021)

The presence of both acidic and basic adsorption sites on the surface of hydroxyapatite [$\text{Ca}_{10}(\text{PO}_4)_6(\text{OH})_2$; HAP] is an interesting property for catalytic applications. Here, we report a density functional theory investigation of the adsorption properties of CO, CO₂, C₂H₂, CH₄, H₂, H₂O, NH₃, SO₂, and BCl₃ on the HAP(0001) surface. All probe molecules have a lower energy when they are adsorbed in the region between the most exposed Ca²⁺ ion (electron acceptor) and a neighboring PO₄³⁻ group, where the O atoms (electron donor) contribute to the stabilization of the adsorbed molecule. By evaluating the redistribution of the electron density and the change of the atomic charges, the Ca²⁺ and PO₄³⁻ sites were identified as Lewis acidic and Lewis basic adsorption sites, respectively, which indicates that simultaneous acid-base interactions occur upon adsorption of all studied probe molecules. All adsorbates interact with the surface via atoms of opposing charges, which enhances the ionic character of molecular bonds by increasing the distinction between cationic and anionic charges within the molecule. Furthermore, molecules with greater ionic character show stronger interaction with the substrate and greater geometric deformation. Although most adsorbed molecules (CO, CO₂, C₂H₂, CH₄, H₂, H₂O, and NH₃) do not show substantial net charge transfer, polarization effects due to the redistribution of charge are observed upon adsorption of all probe molecules. The change in the work function increases linearly with the total change in the surface dipole moment for H₂O, NH₃, SO₂, and BCl₃, while for the remaining systems, the magnitude of the work function change remains more uniform. By identifying the type of interaction between each probe molecule and the HAP(0001) surface, the present study contributes to the understanding of the acid-base properties of the HAP(0001) surface, which we elaborated in a short discussion based on the individual bond orders for the acidic and basic sites.

DOI: [10.1103/PhysRevMaterials.5.075003](https://doi.org/10.1103/PhysRevMaterials.5.075003)

I. INTRODUCTION

Hydroxyapatite [$\text{Ca}_{10}(\text{PO}_4)_6(\text{OH})_2$; HAP] is a mineral known mostly by its biological importance as the primary inorganic constituent of bones and teeth [1,2]. As a bio-material, HAP has been widely studied for applications in tissue engineering [3,4], tumor inhibition [5], controlled drug delivery [6,7], and other medical-related technologies [8,9]. Additionally, owing to the acid-base nature of its surface sites, HAP has been attracting attention in the field of heterogeneous catalysis, especially as a catalyst for the valorization of biomass-derived feedstocks [10].

The continuous improvement of HAP for innovative catalytic applications can benefit from an atomistic understanding of the HAP surface properties. To this end, experiments that analyze the adsorption properties of probe molecules are widely used, e.g., temperature-programmed desorption to measure the surface site density, as well as the binding strength for acidic and basic sites, using NH₃ and CO₂ as probe molecules [11]. Further, spectroscopic analyses of small adsorbates (CO, CO₂, C₂H₂, and H₂O) have been employed for a qualitative description of the active sites [12–14].

Since most catalysts are prepared as powders, numerous crystallographic defects occur in their surfaces, and hence, it is a challenge to obtain atomistic insights from those experimental analyses [15]. In this regard, theoretical studies based on *ab initio* methods have become essential for an in-depth investigation of the HAP surface properties [16].

Several simulations based on density functional theory (DFT) calculations have been reported, along with experimental studies for HAP bulk and surfaces [17–20]. For example, the stability of both hexagonal and monoclinic HAP bulk phases was computed [18], showing that the hexagonal phase is higher in energy by only 11 meV per formula unit, i.e., only 0.25 meV/atom, which is within the limit of DFT implementations. Recently, the primary contribution to the electric polarization in both bulk phases was attributed to the ordered orientation of the OH⁻ groups [20]. Polarization effects were also observed for the HAP(0001) surface, where the electrostatic characteristics differ according to the alignment of OH⁻ groups within the structure [17]. Moreover, the stability of the HAP(0001) surface was tested with respect to the thickness of the slab geometry [21], with the conclusion that a slab model with 4 formula units (88 atoms and 14-Å-thick slab) is sufficient to investigate the adsorption properties of molecular systems. It was also reported that the Ca²⁺ ions are the energetically preferred adsorption sites for H₂O and

*juarez_dasilva@iqsc.usp.br

that neighboring PO_4^{3-} groups could also contribute to the stabilization of the adsorbates [17]. Furthermore, combined DFT calculations and infrared spectroscopy were employed to describe the adsorption of CO, also encountering the electrostatic affinity of the adsorbate for exposed Ca^{2+} ions [19].

The adsorption sites of HAP particles have been described considering two types of adsorption sites, i.e., Lewis acidic (Ca^{2+} ions) and Lewis basic (O atoms of PO_4^{3-} groups) sites [22]. The existence of these surface sites in different proportions has been considered as the dominant factor regulating the catalytic activity and selectivity of HAP and, hence, the key feature for selecting it as a catalyst [23,24]. Despite the aforementioned progress, our understanding of the adsorption properties of the most used probe molecules employed for characterization analyses is still unsatisfactory.

In the present study, we investigate the adsorption properties of a wide range of probe molecules, namely, CO, CO_2 , C_2H_2 , CH_4 , H_2 , H_2O , NH_3 , SO_2 , and BCl_3 , on the HAP(0001) surface by *ab initio* DFT calculations. Our findings indicate that all selected molecules are adsorbed preferentially close to the most exposed Ca^{2+} site, where lateral interactions with neighboring O atoms of PO_4^{3-} groups lead to the stabilization of the adsorbate. Detailed analysis of the adsorption properties revealed that simultaneous acid-base interactions occur in all systems, as anionic and cationic molecular terminations interact with Lewis acidic and Lewis basic surface sites, respectively. Therefore, the choice of probe molecules could affect the distinction between these sites, which is crucial for the interpretation of experimental data. Although no substantial net charge transfer was found for CO, CO_2 , C_2H_2 , CH_4 , H_2 , H_2O , and NH_3 on HAP(0001), polarization effects are observed for all systems, accompanied by changes in the surface dipole moment and work function.

II. THEORETICAL APPROACH AND COMPUTATIONAL DETAILS

A. Total energy calculations

All total energy calculations were based on spin-polarized DFT [25,26] within the semilocal Perdew-Burke-Ernzerhof (PBE) formulation for the exchange-correlation functional [27]. To improve the description of long-range van der Waals (vdW) interactions, we used the vdW D3 correction proposed by Grimme [28]. The Kohn-Sham equations were solved using the projected augmented-wave (PAW) method as implemented in the Vienna *Ab initio* Simulation Package (VASP) [29–31], version 5.4.1. Electron-ion interactions were described by the PAW projectors provided within VASP, in which the valence electrons were described by plane waves. The scalar-relativistic approximation [32,33] was employed, in which spin-orbit coupling was considered for the core states through the PAW projectors and neglected for the valence states due to the negligible effects in the energetic and structural properties. Additional technical PAW details are reported in Sec. S1 in the Supplemental Material (SM) [34].

For all calculations, we employed a plane-wave cutoff energy of 489 eV, which is 12.5% higher than the largest recommended value considering all chemical elements (B, C, Cl, Ca, H, N, O, P, and S). However, because of the slow

convergence of the stress tensor as a function of the number of plane waves, the higher plane-wave cutoff energy of 869 eV was used to obtain the equilibrium lattice constants and internal parameters of the HAP bulk phases. For the Brillouin zone (BZ) integration, we considered only the Γ point for the gas-phase molecules and free atoms owing to the absence of dispersion in the electronic states within the BZ. As for the hexagonal HAP bulk phase with space group $P6_3$, we used a Γ centered Monkhorst-Pack [35] \mathbf{k} mesh of $2 \times 2 \times 3$ for total energy calculations, which was determined from systematic convergence tests as presented in Sec. S2 in the SM [34], and a \mathbf{k} mesh of $4 \times 4 \times 6$ for density of states (DOS) calculations. For the clean surface and adsorption configurations, we employed a \mathbf{k} mesh of $2 \times 2 \times 1$ for total energy calculations and $4 \times 4 \times 1$ for DOS and work function calculations.

The gas-phase molecules were optimized using a 20-Å-cubic-box, while for the free atoms, we used a noncubic box of $20 \times 21 \times 22$ Å to break the symmetry and minimize problems with electronic occupation. For the hexagonal HAP(0001) surface, we employed a slab repeated geometry, which contains a 1×1 surface unit cell with $a_0 = b_0 = 9.497$ Å, a slab with a thickness of four layers [one formula unit $\text{Ca}_5(\text{PO}_4)_3(\text{OH})$ per layer], and a vacuum region of 15 Å. Using the optimized slab, we built the adsorption structures by placing one molecule on each side of the slab in equivalent positions to preserve the inversion symmetry and eliminate the use of dipole corrections. All atoms were allowed to relax through the conjugate gradient algorithm. The equilibrium configurations were obtained once the atomic forces were smaller than $0.025 \text{ eV } \text{Å}^{-1}$ on each atom using a total energy convergence criterion of 10^{-5} eV .

B. Atomic structure configurations

The initial geometries of the isolated gas-phase molecules were obtained from the National Institute of Standards and Technology Computational Chemistry Comparison and Benchmark Database [36] and reoptimized following the above-mentioned computational details. Regarding the hexagonal HAP bulk unit cell (Fig. 1) the initial configuration was constructed from experimental measurements [37] by reducing the crystal system from space group $P6_3/m$ to space group $P6_3$ as discussed further below.

In the formation of a surface, numerous configurations can be found based on the chemical potential of its building elements. A theoretical energetic analysis of different vacuum-exposed HAP surfaces was discussed in detail elsewhere [16], and hence, it is not discussed here. In the present study, having optimized the $P6_3$ HAP bulk structure, we considered only the stoichiometric termination for the HAP(0001) surface, previously reported as the most stable termination from a thermodynamic standpoint [38–40]. Furthermore, concerning our interest in evaluating the acid-base properties of the HAP surface, the well-defined structure of the HAP(0001) surface accommodates interspersed vacuum-exposed Ca^{2+} ions and PO_4^{3-} groups that make this termination suitable to simulate positively and negatively charged adsorption sites. This choice was also motivated by experimental [12–14,41] and theoretical [17,19,21] studies

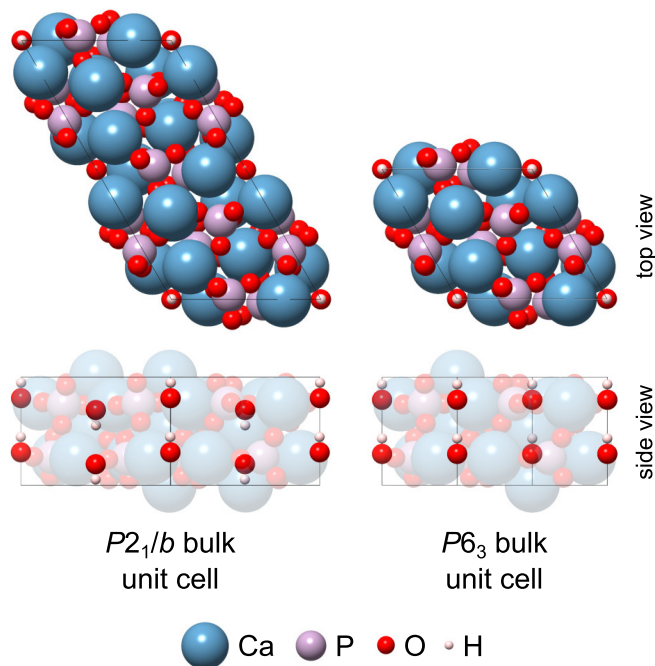


FIG. 1. Bulk phases of stoichiometric hydroxyapatite, namely, the $P2_1/b$ monoclinic and $P6_3$ hexagonal phases. The side view of each phase emphasizes the orientation of the OH^- groups along the $[0001]$ direction. Additional details on the crystallographic positions for the $P6_3$ structure are provided in the SM [34], Sec. S4.

that have investigated these vacuum-exposed species as Lewis acidic and Lewis basic adsorption sites, respectively.

The initial adsorption configurations for all systems were obtained by placing the molecules above different adsorption sites at about 2 Å from the relaxed clean surface on each side of the slab. The relaxed HAP(0001) is slightly corrugated due to the presence of the Ca^{2+} ions displaced above the surface layer (Fig. 2), which introduces further difficulties in identifying the lowest-energy configurations of the adsorbed molecules. However, given the small size of the selected molecules and the symmetrical distribution of the adsorption

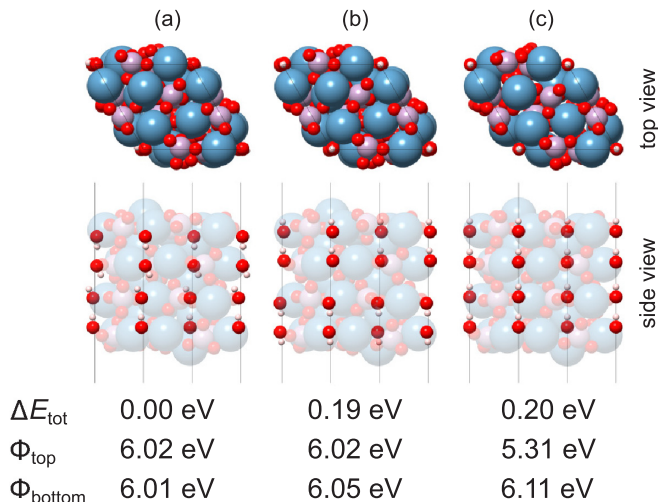


FIG. 2. Orientation of the OH^- groups across the HAP(0001) slab model. The total energy relative to the lowest-energy configuration, ΔE_{tot} , is given below each model. The work functions of the top and bottom surfaces are indicated as Φ_{top} and Φ_{bottom} .

sites, we generated a set of adsorption configurations sufficient to explore different HAP(0001) adsorption sites at a reasonable computational cost. Hence, for each adsorption system Mol/HAP , where $Mol = \text{CO}, \text{CO}_2, \text{C}_2\text{H}_2, \text{CH}_4, \text{H}_2, \text{H}_2\text{O}, \text{NH}_3, \text{SO}_2$, or BCl_3 , we generated a total of 12 configurations. The atomic coordinates for the optimized lowest-energy adsorption structures are provided in the SM [34], Sec. S10.

III. RESULTS AND DISCUSSION

A. Gas-phase molecules

For gas-phase molecules, the most important properties are summarized in Table I. Compared to experimentally reported values [42–44], the PBE + D3 bond lengths and bond angles deviated by less than 2%, while the binding energies exhibited larger deviations, from 1.04% for H_2 up to 13.34% for BCl_3 . The total dipole moment and the atomic charges were calculated using the density-derived electrostatic and chemical

TABLE I. Structural, energetic, and electronic properties of the gas-phase molecules. Average bond length, d_0 (Å); average bond angle, α_0 (°); binding energy per atom, E_b (eV); total dipole moment, μ_0^{Mol} (D); and average atomic charges of cationic and anionic atoms (indicated by superscripts) within each molecule, respectively, Q_+^{Mol} and Q_-^{Mol} (e). For C_2H_2 , d_0 corresponds to the $\text{C}\equiv\text{C}$ bond, while the optimized C–H bond measured 1.07 Å, and α_0 corresponds to the average CCH angle. Values in parentheses correspond to the percentage deviations relative to experimental results [36,42–44].

Property	CO	CO ₂	C ₂ H ₂	CH ₄	H ₂	H ₂ O	NH ₃	SO ₂	BCl ₃
d_0	1.14 (0.89)	1.17 (1.10)	1.21 (0.34)	1.10 (0.87)	0.75 (1.56)	0.97 (1.38)	1.02 (1.10)	1.45 (1.61)	1.75 (0.30)
α_0		180.00 (0.00)	180.00 (0.00)	109.47 (0.00)		104.09 (−0.40)	106.00 (−0.65)	119.35 (0.01)	120.00 (0.00)
E_b	−5.82 (4.62)	−6.00 (8.18)	−4.49 (5.91)	−3.64 (5.77)	−2.26 (1.04)	−3.38 (5.90)	−3.27 (5.52)	−4.05 (10.10)	−3.71 (13.34)
μ_0^{Mol}	0.18 (62.75)	0.00 (0.00)	0.00 (0.00)	0.00 (0.00)	0.00 (0.00)	1.81 (−2.30)	1.50 (2.34)	1.55 (−4.80)	0.00 (0.00)
Q_+^{Mol}	0.11 ^C	0.72 ^C	0.22 ^H	0.15 ^H	0.00 ^H	0.38 ^H	0.29 ^H	0.74 ^S	0.48 ^B
Q_-^{Mol}	−0.11 ^O	−0.36 ^O	−0.22 ^C	−0.60 ^C	0.00 ^H	−0.76 ^O	−0.88 ^N	−0.37 ^O	−0.16 ^{Cl}

(DDEC6) approach [45,46]. For nonpolar molecules (CO_2 , C_2H_2 , CH_4 , H_2 , and BCl_3), the total dipole moment was null for all cases, while for polar molecules (H_2O , NH_3 , and SO_2), it deviated within $\pm 5\%$ relative to experimental results [44]. Regarding the noticeable overestimation of the total dipole moment for the CO molecule, previous studies [47,48] also encountered similar results. For the atomic charges, the calculated values are consistent with the tendencies expected from the electronegativity difference between the cationic and the anionic atoms within each molecule. We report additional theoretical results to reinforce the agreement with experimental results in the SM [34], Sec. S5.

B. Bulk properties

The HAP crystal exists naturally in two different space group symmetries, namely, the $P6_3/m$ hexagonal [37] and the $P2_1/b$ monoclinic [49] structures (Fig. 1). The major difference between the two phases lies in the orientation of the OH^- groups along the [0001] direction, which doubles the number of formula units within the monoclinic unit cell compared with the hexagonal one. Most studies identify a statistical disorder of the OH^- groups in the hexagonal structure [50], whereas in the monoclinic structure, the OH^- groups are ordered upwards in one column and downwards in the nearest-neighbor column [49]. Although the OH^- misalignment in the hexagonal HAP is adequately described by fractional occupations within the $P6_3/m$ space group, the equivalent positions above/below the mirror plane generate a duplication of each OH^- that breaks the HAP stoichiometry in computational simulations. To overcome this limitation, we reduced the crystal symmetry to $P6_3$ while fixing the alignment of the OH^- groups to maintain the correct stoichiometry [38,39,51].

From the optimization of the lattice parameters, we found $a_0 = b_0 = 9.497 \text{ \AA}$ and $c_0 = 6.863 \text{ \AA}$ for the hexagonal HAP structure, while $a_0 = 9.475 \text{ \AA}$, $b_0 = 2a_0$, and $c_0 = 6.880 \text{ \AA}$ for the monoclinic HAP structure. Upon comparison with experimental measurements [37,49], the unit cell of both hexagonal and monoclinic HAP slightly expanded in the a_0 direction (by 0.84% and 0.52%, respectively) and contracted in the c_0 direction (by -0.17% and -0.02% , respectively). Moreover, the addition of the vdW D3 correction improved the agreement with the experimental results due to the attractive nature of the vdW correction and common overestimation of lattice parameters by the PBE functional. The slightly greater deviations observed for the hexagonal phase are likely connected to the imposed alignment of the OH^- groups. Compared to other DFT-PBE studies [52–54], our results deviated by less than 1%, thus indicating that both bulk structures are accurately represented.

Although monoclinic HAP had been reported as the most stable form, the prominent use of hexagonal HAP in biomedical [55] and catalytic [10] applications has made the hexagonal phase more relevant and frequently more studied [56]. Our results indicate that the monoclinic phase is lower in energy compared to hexagonal HAP by 16.95 meV per formula unit (0.77 meV per atom), which is in qualitative agreement with experimental [57] and theoretical [18,38,39] results. However, we should keep in mind that the relative energy difference between the two structures is in the limit of

the accuracy of the present calculations. In the present study, we selected the $P6_3$ hexagonal phase structure to accurately model HAP at a more feasible computational cost.

C. Clean surface properties

The thickness of the slab was determined from evaluating the convergence of surface properties with respect to the number of layers stacked along the direction perpendicular to the HAP(0001) surface, the z direction in our framework. From the slab thickness calculations, we found that four layers is sufficient to converge both energetic and geometric properties, which is consistent with previous studies [17,19,21,58,59]. The construction of the slab model directly from the hexagonal $P6_3$ bulk unit cell originates unequal top and bottom (0001) surfaces because of the imposed OH^- alignment across the slab, as indicated in Fig. 2(c), and hence, it would require the addition of dipole corrections to avoid flow charge across the slab. To obtain equivalent surfaces on both sides of the slab, we built two additional configurations by flipping the orientation of the OH^- groups, as indicated in Figs. 2(a) and 2(b). Thus, three models are discussed for the HAP(0001) surface (Fig. 2).

The OH^- alignment can strongly affect the structural [60] and electronic [17,21] properties of the HAP(0001) surface. For example, we obtained different interlayer relaxations of -10.62% (-25.07%), for the top (bottom) outermost layers of Ca^{2+} ions in the slab model in Fig. 2(c), OH-OH-OH-OH , whereas nearly identical relaxations on both sides of the slab appeared when the OH^- groups were aligned as in Fig. 2(a), OH-OH-HO-HO , and Fig. 2(b), HO-HO-OH-OH , respectively, -25.01% (-24.89%) and -22.25% (-21.93%) for the top (bottom) outermost layers of Ca^{2+} ions. For both slabs, the inversion symmetry was initially broken to check possible different relaxations on both sides of the slab, which explains the tiny differences.

Additionally, the asymmetric slab, which is shown in Fig. 2(c), yields a difference of 0.80 eV between the top and the bottom surface work functions, Φ_{top} and Φ_{bottom} , while in the symmetric slab models the differences are tiny, e.g., 0.01 and 0.03 eV. The change in the OH^- alignment results in equivalent surfaces on both sides of the slab, which exempts the use of dipole corrections because of the null net dipole moment within the supercell. By evaluating the alternative OH^- alignments, we found that the slab model in Fig. 2(a) was the most stable configuration, having the O atoms of the OH^- groups pointed towards the vacuum; hence, this model was used as the substrate throughout all adsorption systems. Additional results using different number of layers are reported in the SM [34], Sec. S6.

The atomic displacements observed on the HAP(0001) surface resulted from the change in coordination of the vacuum-exposed atoms compared to the bulk geometry. As indicated in Table II, the interlayer distance, d_{\perp} , for Ca^{2+} ions contracted by 25%; for OH^- groups, it contracted by 17%, followed by a misalignment along the z direction [Fig. 2(a)], to minimize the repulsion between neighboring H atoms [17]; and for the PO_4^{3-} groups, their rearrangement resulted in a contraction by 20% of the O layers, which increased the number of accessible O atoms on the HAP(0001) surface. As

TABLE II. Geometric properties of $P6_3$ bulk HAP, clean HAP(0001), and Mol /HAP adsorbed systems. Interlayer distance between the two outermost layers of the substrate, d_{\perp}^{Ca} , d_{\perp}^{P} , d_{\perp}^{O} , and $d_{\perp}^{\text{O(H)}}$ (Å); shortest distance from atoms in the molecule (indicated by superscripts) to substrate Ca^{2+} ions, $d^{\text{Mol-Ca}}$ (Å), and to PO_4^{3-} groups, $d^{\text{Mol-O}}$ (Å); change in the average bond length, Δd_0 (%), and change in the average bond angle, $\Delta\alpha_0$ (%), with respect to the gas-phase molecules.

System	d_{\perp}^{Ca}	d_{\perp}^{P}	d_{\perp}^{O}	$d_{\perp}^{\text{O(H)}}$	$d^{\text{Mol-Ca}}$	$d^{\text{Mol-O}}$	Δd_0	$\Delta\alpha_0$
Bulk	1.71	3.43	1.25	3.43				
HAP(0001)	1.28	3.67	1.00	2.86				
CO/HAP	1.32	3.65	0.97	2.85	2.74 ^C	2.95 ^C	-0.38	
CO ₂ /HAP	1.35	3.64	0.92	2.86	2.51 ^O	2.83 ^C	0.01	-2.60
C ₂ H ₂ /HAP	1.38	3.61	0.88	2.90	2.91 ^C	2.12 ^H	0.58	-4.38
CH ₄ /HAP	1.35	3.64	0.93	2.86	2.98 ^C	2.46 ^H	0.37	-0.04
H ₂ /HAP	1.30	3.66	0.99	2.86	2.69 ^H	2.64 ^H	1.05	
H ₂ O/HAP	1.44	3.62	0.90	2.88	2.36 ^O	1.60 ^H	2.87	1.96
NH ₃ /HAP	1.39	3.65	0.96	2.86	2.51 ^N	1.93 ^H	0.62	0.45
SO ₂ /HAP	1.42	3.61	0.93	2.85	2.35 ^O	2.04 ^S	2.27	-7.59
BCl ₃ /HAP	1.52	3.53	0.80	2.95	2.76 ^{Cl}	1.44 ^B	8.23	-8.46

expected from a well-converged surface slab, the inner layers showed only minor modifications of their atomic positions compared to the crystalline structure, indicating a bulklike behavior. A visual representation of the HAP layers and their respective distances are provided in Fig. 3.

D. Adsorbed systems

In this section, we discuss the PBE + D3 results obtained for the optimized lowest-energy adsorption structures represented in Fig. 4. Additional degenerate and higher-energy configurations are available in the SM [34], Sec. S7.

1. Adsorption site preference

All adsorbates on the HAP(0001) surface showed an energetic preference for the vicinity of the most exposed Ca^{2+} ions where neighboring O atoms of PO_4^{3-} groups played an important role in stabilizing and determining the orientation of the molecules (Fig. 4). In this respect, HAP(0001) presented a delicate balance of electrostatic attraction in the system that

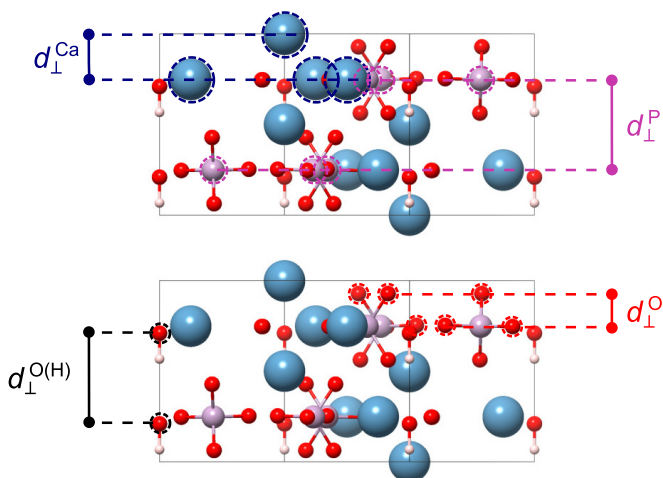


FIG. 3. Schematic side view of HAP layers, in which d_{\perp}^i indicates the interlayer distance relative to the chemical species $i = \{\text{Ca}, \text{P}, \text{O}, \text{O(H)}\}$ in the substrate.

maximizes the interaction of the cationic and anionic regions of the molecule with adsorption sites of opposite charges.

For all selected probe molecules, the cationic atoms within the molecule interacted mostly with the O atoms of PO_4^{3-} groups, Lewis basic sites, while the anionic atoms within each molecule were more attracted by the Ca^{2+} ions, Lewis acidic sites. This trend can be seen in the shortest distances between atoms in molecules and the substrate. The only exception occurred for CO, which, due to the charge of the highest occupied molecular orbital (HOMO) being mainly located around the C atom [47], was primarily adsorbed by its carbon atom to both Lewis acidic and Lewis basic sites. This adsorption mode is consistent with previous studies for a wide range of surfaces [19,59,61,62]. Although OH^- groups emerging from HAP OH^- tunnels have been experimentally identified as negatively charged surface sites [12,13,41], the OH^- groups in our HAP(0001) model are less exposed to the surface, compared to the Ca^{2+} ions and PO_4^{3-} groups, due to the rearrangement of the surface layers upon structural optimization; however, as discussed in previous sections, they play a crucial role in the properties of the bulk and clean surface.

2. Adsorption and interaction energies

To characterize the strength of the interaction between the probe molecules and the HAP(0001) surface, we evaluated the adsorption energy as

$$E_{\text{ad}} = \frac{1}{2}(E_{\text{tot}}^{\text{Mol/Sub}} - 2E_{\text{tot}}^{\text{Mol}} - E_{\text{tot}}^{\text{Sub}}), \quad (1)$$

where $E_{\text{tot}}^{\text{Mol/Sub}}$ is the total energy of the adsorbed system, $E_{\text{tot}}^{\text{Mol}}$ is the total energy of the gas-phase molecule, and $E_{\text{tot}}^{\text{Sub}}$ is the total energy of the clean HAP(0001) substrate. Moreover, we calculated the interaction energy, E_{int} , which is related to E_{ad} by

$$E_{\text{int}} = E_{\text{ad}} - \frac{1}{2}\Delta E_{\text{tot}}^{\text{Mol}} - \frac{1}{2}\Delta E_{\text{tot}}^{\text{Sub}}, \quad (2)$$

where $\Delta E_{\text{tot}}^{\text{Mol}}$ and $\Delta E_{\text{tot}}^{\text{Sub}}$ are the deformation energies of the molecule and the substrate, i.e., the energy difference between the isolated systems frozen in their adsorbed and optimized geometries. The factors $\frac{1}{2}$ in Eqs. (1) and (2) are consequences

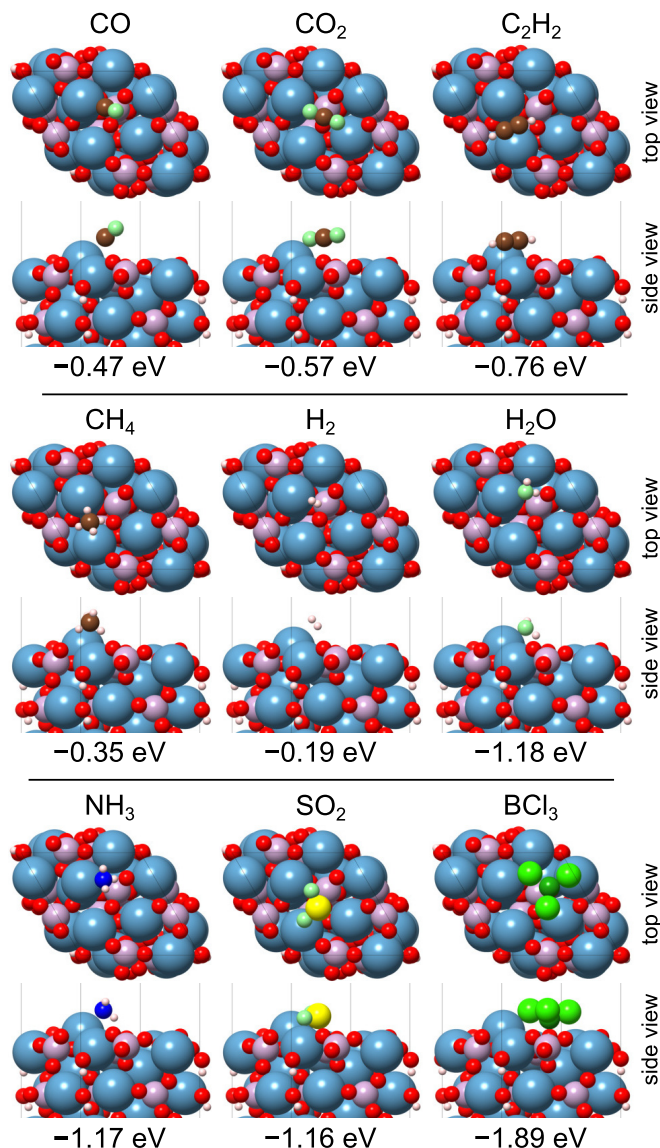


FIG. 4. Optimized lowest-energy configurations of adsorbed molecules on HAP(0001). The adsorption energy, E_{ad} (eV), is given below each structure. To facilitate visualization, the oxygen atoms in the molecules are depicted as light-green spheres.

of adsorbing molecules on both sides of the slab. PBE + D3 results are shown in Fig. 4 and summarized in Table III.

The relatively large range of E_{ad} values indicates that the adsorption was strongly connected to the physical properties of each molecule and the adsorption site. H_2 and CH_4 showed the weakest interactions with the substrate since both molecules are nonpolar and have a high covalent character. For CO, the electronic charge distribution mainly located around the C atom [47] generates a permanent dipole moment that increased its interaction with the substrate. Meanwhile, when the adsorption occurred via the O atom, the interaction was higher in energy by only 0.39 eV.

Although CO_2 and C_2H_2 are nonpolar, both molecules have polar bonds within their structures that contributed to stronger interactions with the surface. For CO_2 , the electronegativity of O atoms induces a positive partial charge on

TABLE III. Energetic properties of the adsorbed systems. Adsorption energy, E_{ad} (eV); interaction energy, E_{int} (eV); and deformation energies for the isolated molecule, $\Delta E_{\text{tot}}^{\text{Mol}}$ (eV), and isolated substrate, $\Delta E_{\text{tot}}^{\text{Sub}}$ (eV).

System	E_{ad}	E_{int}	$\Delta E_{\text{tot}}^{\text{Mol}}$	$\Delta E_{\text{tot}}^{\text{Sub}}$
CO/HAP	-0.47	-0.49	0.00	0.02
CO_2 /HAP	-0.57	-0.65	0.03	0.05
C_2H_2 /HAP	-0.76	-0.92	0.03	0.13
CH_4 /HAP	-0.35	-0.42	0.02	0.05
H_2 /HAP	-0.19	-0.19	0.00	0.00
H_2O /HAP	-1.18	-1.41	0.07	0.16
NH_3 /HAP	-1.17	-1.25	0.01	0.07
SO_2 /HAP	-1.16	-1.85	0.16	0.52
BCl_3 /HAP	-1.89	-4.50	1.70	0.91

the C atom, while for C_2H_2 the triple $\text{C}\equiv\text{C}$ bond generates an accumulation of charge at the center of the molecule. The magnitude of E_{ad} and E_{int} increased further for the polar molecules with a permanent dipole moment and higher ionic character (H_2O , NH_3 , and SO_2), while the largest values were observed for BCl_3 , which has the strongest Lewis acidity compared to the other probe molecules. Compared with previous DFT studies, we obtained lower adsorption energies. The reported values for the adsorption energy of CO [19] and H_2O [17] on the HAP(0001) surface are -0.32 and -1.14 eV, respectively.

For all systems, the E_{int} values were greater than the E_{ad} because of the geometric changes that occurred upon adsorption. In general, the geometric perturbations were directly proportional to the strength of the adsorption, i.e., for systems with lower adsorption energies, smaller differences between E_{int} and E_{ad} were observed; otherwise, as the adsorption energy increased, so did the difference $E_{\text{int}} - E_{\text{ad}}$. For most systems the deformation energy of the substrate, $\Delta E_{\text{tot}}^{\text{Sub}}$, was greater than the deformation energy of the adsorbed molecule, $\Delta E_{\text{tot}}^{\text{Mol}}$, suggesting that the geometric deformations of the substrate contributed more to the structural stabilization of the adsorbed systems. In contrast, the deformation energy of BCl_3 was greater than the deformation energy of the substrate, indicating that the structure of BCl_3 is more affected than the structure of the substrate upon adsorption. The structural changes due to adsorption are listed in Table II.

3. Geometric properties

The geometric properties used to characterize the adsorbed systems are summarized in Table II, while a visual representation of the interlayer distances is provided in Fig. 3. For all adsorbed systems, the presence of the adsorbate increased the coordination of vacuum-exposed atoms, contributing to their electrostatic stabilization. This effect is more pronounced for the outermost Ca^{2+} layers, which expanded vertically compared to the clean HAP(0001). The most significant change occurred for BCl_3 : the molecule with the greatest adsorption energy and shortest distance from the substrate. In contrast, for all adsorbed systems the outermost O layers contracted compared to the clean HAP(0001). The rearrangement of O atoms on the surface follows the shift of PO_4^{3-} tetrahedrons

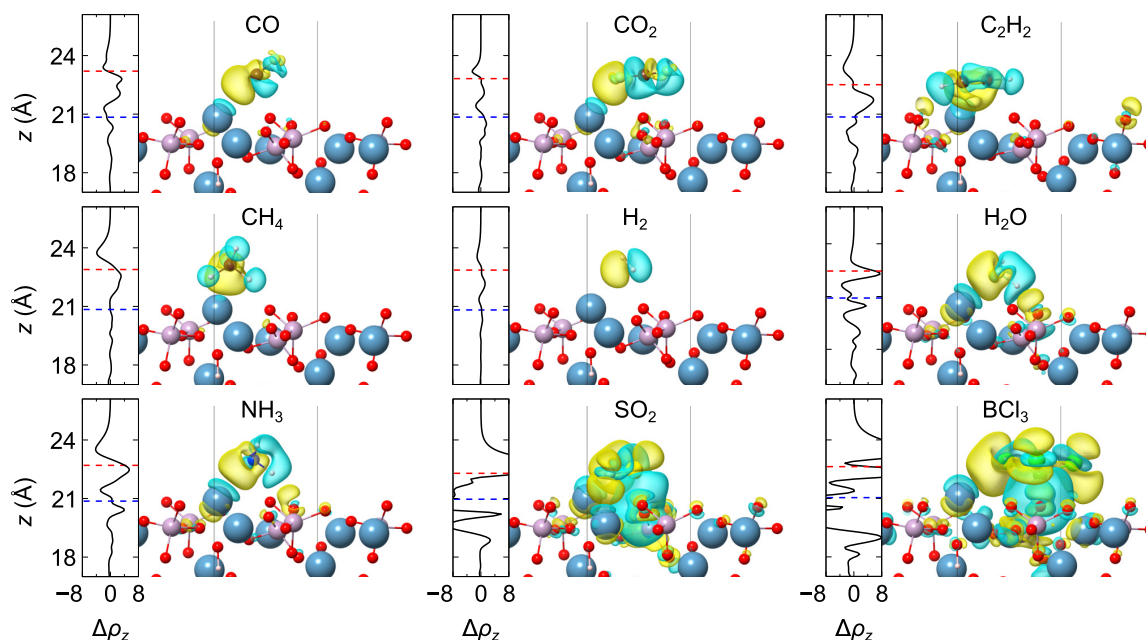


FIG. 5. Electron density difference isosurfaces ($0.01 e \text{ \AA}^{-3}$) for the lowest-energy adsorption configurations. Yellow and blue regions indicate accumulation and depletion of charge, respectively. $\Delta\rho_z$ ($e \text{ \AA}^{-1}$) is the plane-average electron density along the direction perpendicular to the surface, z direction. The dashed red and blue lines indicate, respectively, the center of mass of the adsorbed molecule and the position of the most exposed Ca^{2+} on HAP(0001).

towards the center of the slab, as observed by the reduced distance between the layers of P atoms.

For most systems, the shortest distance between the molecule and the substrate occurred via the O atoms of PO_4^{3-} groups; however, for CO and CO_2 , the shortest distance appeared between the molecule and the most exposed Ca^{2+} ion on the surface. Moreover, the distance between the molecule and the substrate was inversely proportional to the adsorption strength, that is, molecules such as BCl_3 , SO_2 , H_2O , and NH_3 showed greater E_{ad} values and, consequently, smaller distances from the substrate.

Regarding the noticeable overestimation of the CO total dipole moment, in which the C–O bond becomes stronger when the molecule interacts with the surface via its HOMO [47,63]. The geometry of BCl_3 was the most affected upon adsorption, followed by H_2O and SO_2 . Another notable aspect of geometric deformation was observed for NH_3 , which, despite having an adsorption energy in the same range as that of the other polar molecules, displayed geometric deformation similar to that of nonpolar molecules with a lower adsorption energy.

The change in the molecular angles varied according to the electronic effects for each molecule. For BCl_3 , there was a rearrangement from a planar structure to a trigonal pyramid with decreased ClBCl angles, due to the increased occupation of its molecular orbitals [64]. For CO_2 , a similar behavior is also possible with a bent OCO configuration [65], however, this was not observed for our CO_2/HAP systems owing to the lack of net charge transferred between the adsorbed molecule and the substrate. The change in the molecular angles did not correlate with the adsorption strength; H_2O , NH_3 , and SO_2 showed similar E_{ad} values, yet their angular deformations are completely distinct.

4. Electron density difference and atomic charges

The electron density difference upon adsorption was calculated as

$$\Delta\rho = \rho^{\text{Mol/Sub}} - \rho^{\text{Mol}} - \rho^{\text{Sub}}, \quad (3)$$

where $\rho^{\text{Mol/Sub}}$ is the electron density of the adsorbed system, while ρ^{Mol} and ρ^{Sub} are the electron densities of the isolated molecule and the isolated substrate frozen in their respective adsorbed geometries. Figure 5 depicts the isosurfaces and plane-average electron density along the z direction, while the atomic charges computed using the DDEC6 approach [45,46] are listed in Table IV.

The electron density difference revealed a charge accumulation near the most exposed Ca^{2+} ion and small perturbations around neighboring substrate atoms. As the adsorption strength increased, the extent of the electron density perturbations tended to increase spatially; for example, significant charge perturbations could be observed in the substrate of SO_2 and BCl_3 systems at the selected isosurface level. The charge accumulation next to the Ca^{2+} ion could be related to its net positive atomic charge, which generates a capacity to accept charge in the region via electrostatic interaction and, thus, indicates a Lewis acidic character for this adsorption site. For opposite reasons, the neighboring O atoms of PO_4^{3-} could be considered adsorption sites with a Lewis basic character, as their net negative atomic charges tended to attract the portion of the molecules with charge depletion. Moreover, in all systems containing H atoms, there was a charge depletion around them, which could be related to the weakening of the –H bonds. Despite the tangled aspect of the isosurfaces, the earlier observations can also be applied for SO_2 and BCl_3

TABLE IV. Electronic properties of the adsorbed systems. Charge variation of the substrate atoms, ΔQ^{Ca} , ΔQ^{P} , and ΔQ^{O} (e); total charge variation of the substrate, ΔQ^{Sub} (e); charge variation of cationic and anionic atoms (indicated by superscripts) within the molecule, ΔQ_+^{Mol} and ΔQ_-^{Mol} (e), respectively; total adsorption-induced change in the surface dipole moment, $\Delta\mu_z$ (D); and change in the work function, $\Delta\Phi$ (eV).

System	ΔQ^{Ca}	ΔQ^{P}	ΔQ^{O}	ΔQ^{Sub}	ΔQ_+^{Mol}	ΔQ_-^{Mol}	$\Delta\mu_z$	$\Delta\Phi$
CO/HAP	-0.11	-0.02	0.02	-0.05	-0.01 ^C	0.06 ^O	-1.53	-0.14
CO ₂ /HAP	-0.02	-0.02	0.03	-0.03	0.07 ^C	-0.10 ^O	-0.42	-0.16
C ₂ H ₂ /HAP	-0.06	-0.02	0.05	-0.05	0.03 ^H	-0.01 ^C	-0.49	-0.19
CH ₄ /HAP	-0.03	-0.02	0.04	-0.03	0.02 ^H	-0.05 ^C	-0.15	-0.23
H ₂ /HAP	-0.04	-0.02	0.04	-0.02	0.04 ^H	-0.02 ^H	-0.55	-0.08
H ₂ O/HAP	-0.01	-0.01	0.04	0.01	0.04 ^H	-0.09 ^O	1.97	-0.14
NH ₃ /HAP	-0.06	-0.01	0.02	-0.05	0.04 ^H	-0.07 ^N	-0.42	-0.65
SO ₂ /HAP	-0.01	-0.03	0.21	0.24	0.15 ^S	-0.20 ^O	10.15	0.37
BCl ₃ /HAP	-0.03	0.04	0.20	0.33	0.18 ^B	-0.17 ^{Cl}	14.49	1.14

adsorbed systems. Additional views of the electron density difference isosurfaces are available in the SM [34], Sec. S7.

For all systems, the charge of the most exposed Ca²⁺ ion decreased, while the charge of its neighboring O atom increased. These charge variations could also reinforce their potential as Lewis acidic and Lewis basic adsorption sites, respectively. Concerning the atomic charges of the adsorbates, the redistribution of the electron density enhances the ionic character in the molecular bonds by increasing the distinction of cationic and anionic atoms, i.e., their charges become more positive or more negative depending on the electronegativity of each element. As mentioned earlier, the CO molecule interacts with the surface via its HOMO, which is mainly located on the carbon atom. The CO electron density difference isosurfaces show a significant charge accumulation around the carbon atom and a charge depletion near the oxygen atom, which is consistent with the observed negative and positive charge variations for the respective atoms.

5. Dipole moments and work function

From the electron density difference, we observed that the presence of the adsorbate produced an electronic redistribution on the HAP(0001) surface that also impacts the surface dipole moment. The total adsorption-induced change of the surface dipole moment, $\Delta\mu_z$, was calculated as

$$\Delta\mu_z = \Delta\mu_z^{\text{Mol/Sub}} + \mu_z^{\text{Mol}} + \mu_z^{\text{Sub}} - \mu_{0,z}^{\text{Sub}}, \quad (4)$$

where $\Delta\mu_z^{\text{Mol/Sub}}$ is the change of the surface dipole related to the charge redistribution, μ_z^{Mol} is the dipole moment of the adsorbed molecule, μ_z^{Sub} is the dipole moment of the substrate in the presence of the adsorbate, and $\mu_{0,z}^{\text{Sub}}$ is the dipole moment of the clean substrate. Equation (4) shows that there are three contributions to the change of the surface dipole moment. The first contribution comes from the charge rearrangement induced by the adsorbate [66], given by

$$\Delta\mu_z^{\text{Mol/Sub}} = \int_{z_0}^{z_1} z \Delta\rho_z dz, \quad (5)$$

where z_0 and z_1 correspond to the position at the center of the substrate and the position at the center of the vacuum region of the slab model, respectively. $\Delta\rho_z$ is the electron density

difference, Eq. (3), averaged over the xy plane along the z direction.

The second contribution is due to the dipole of the adsorbed molecule, while the third contribution is due to the displacement of the atomic positions in the substrate, given by the difference between the dipole moment of the substrate after and before adsorption. We emphasize that the reported dipole moments of the adsorbed molecule and the substrate, calculated using the DDEC6 atomic charges, correspond only to the vector component along the z direction. The change in the surface dipole moment determines the change in the work function, $\Delta\Phi$, calculated as the difference between the work function of the adsorbed system and that of the clean substrate. Table IV and Fig. 6 show the results for work function and surface dipole changes.

The change in the work function increased linearly with the total change in the surface dipole moment. This linear correlation was mostly observed for H₂O, NH₃, SO₂, and BCl₃ adsorption systems, where the presence of the adsorbed molecules significantly affected the geometric and electronic properties of the substrate. For the remaining systems, the magnitude of the work function change was very similar, which could be related to the reduced amount of charge transferred and less expressive polarization effects. Figure 6(d) shows that the change in the surface dipole moment determined the change in the work function, having the displacement of the atomic positions in the substrate as the main contribution [Fig. 6(c)]. In the presence of the adsorbate, the atomic positions of the substrate were reorganized to accommodate the molecule and reduce the magnitude of the electrostatic repulsion. Moreover, polarization effects caused by the charge redistribution and the dipole moment of the adsorbed molecule also influenced the surface dipole moment.

For comparison, we have also examined the linear relationship between the work function and the surface dipole changes from electrostatics [67], given by

$$\Delta\Phi = \frac{12\pi\Theta}{A} \Delta\mu_z, \quad (6)$$

where Θ is the surface coverage in monolayers (ML), A is the area of the 1×1 surface unit cell in \AA^{-2} , $\Delta\Phi$ is the work function change in eV, and $\Delta\mu_z$ is the surface dipole change in Debyes (D). Equation (6) shows that the work

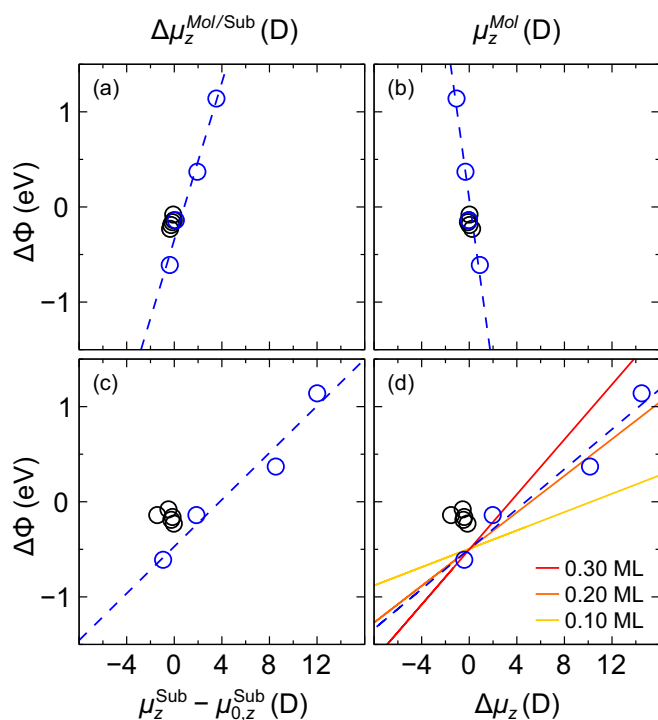


FIG. 6. Relationship between work function and surface dipole changes. Dashed lines indicate the linear regression considering only the values for H_2O , NH_3 , SO_2 , and BCl_3 adsorption systems, shown in blue. Solid lines show the effect of different surface coverages on the linear regression slope. Yellow, orange, and red lines represent $\Theta = 0.10$, 0.20 , and 0.30 ML, respectively.

function and the surface dipole changes are proportional, with a predetermined slope of 0.48 eV/D for $\Theta = 1.00$. The linear regression [Fig. 6(d)] for the H_2O , NH_3 , SO_2 , and BCl_3 adsorption systems has a slope of 0.10 eV/D. This difference can be attributed to the fact that our investigated systems have a lower surface coverage, which is one molecule per 1×1 surface unit cell. By adjusting the value of Θ in Eq. (6), the surface coverage in our adsorption systems was estimated to be 0.22 ML. Details on the calculation of the surface dipole change as well as the numerical values of each contribution are provided in the SM [34], Sec. S9.

6. Density of states

To investigate the role of the electronic states in the Mol/HAP systems, we calculated the local density of states (LDOS) averaged per atom for the lowest-energy adsorption configurations, as shown in Fig. 7. For the adsorbed molecules, the LDOS values were averaged per cationic and anionic atoms, while for the substrate, the LDOS values were averaged per vacuum-exposed Ca, O, and P atoms on the HAP(0001) surface.

For the adsorption of CO , CO_2 , C_2H_2 , CH_4 , and H_2 , we noted a broadening in the molecular electronic states. The more noticeable broadening of C_2H_2 could be related to the perturbation in the electron density of the $\text{C}\equiv\text{C}$ bond due to the lateral interaction with the Ca^{2+} ion, thus showing that the molecular orientation could affect the superposition and hybridization of molecular bonding orbitals. Analogously, the

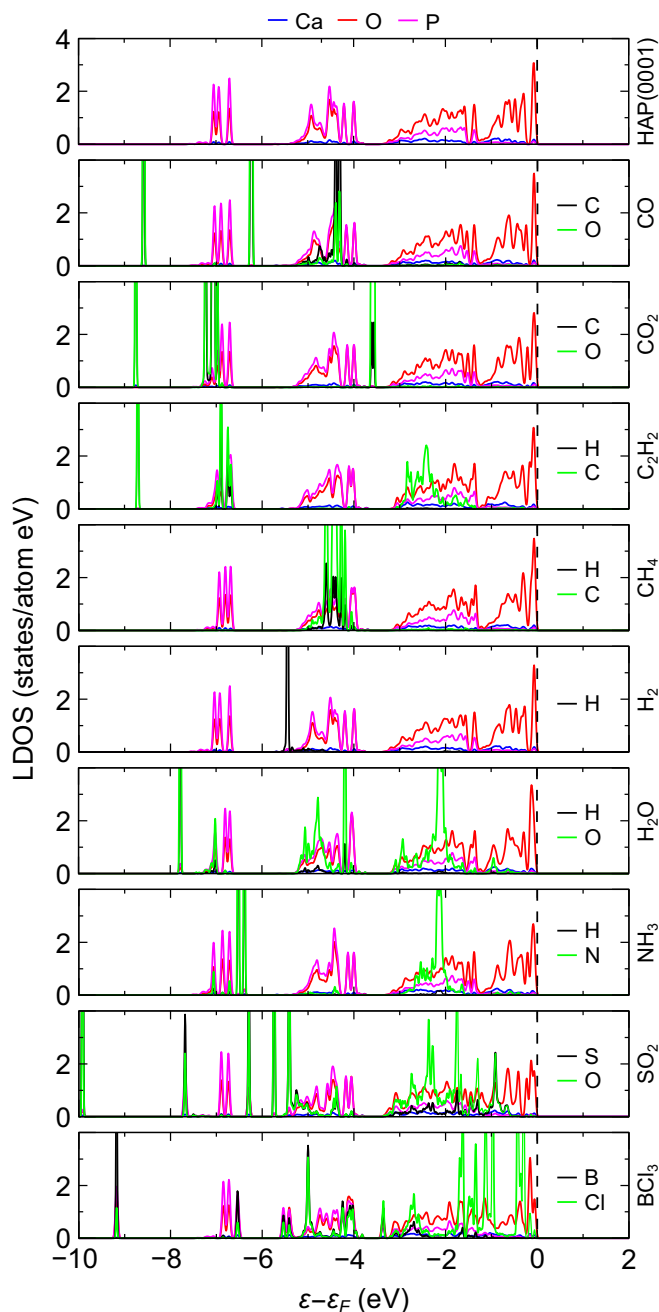


FIG. 7. Local density of states (LDOS) averaged per atom for the lowest-energy adsorption structures. Blue, red, and pink lines refer, respectively, to vacuum-exposed Ca, O, and P atoms on the HAP(0001) surface, while black and green lines refer to atoms within the adsorbed molecules. The dashed vertical lines indicate the Fermi energy.

molecular orientation effect could be demonstrated by the CO adsorption, in which the electronic states of the molecule were stabilized when CO was adsorbed via its C atom.

For the adsorption systems with greater adsorption energies (H_2O , NH_3 , SO_2 , and BCl_3), the broadening of the molecular states was more expressive, which could be attributed to the increase in molecular dipoles and the enhancement of the atomic charges in the adsorbed molecules.

TABLE V. Acid-base character of the preferential adsorption site based on bond order (BO) values. BO between the atoms within the adsorbed molecule (indicated by superscripts) and the Lewis acidic (Ca^{2+}) and Lewis basic (PO_4^{3-}) adsorption sites, BO^{Ca} and BO^{O} , respectively. The "site" column indicates the prevailing interaction upon adsorption.

System	BO^{Ca}	BO^{O}	Site
CO/HAP	0.18 ^C	0.06 ^C	Acidic
CO ₂ /HAP	0.16 ^O	0.05 ^C	Acidic
C ₂ H ₂ /HAP	0.09 ^C	0.08 ^H	Acidic/basic
CH ₄ /HAP	0.07 ^C	0.05 ^H	Acidic/basic
H ₂ /HAP	0.04 ^H	0.04 ^H	Acidic/basic
H ₂ O/HAP	0.23 ^O	0.20 ^H	Acidic/basic
NH ₃ /HAP	0.22 ^N	0.11 ^H	Acidic
SO ₂ /HAP	0.23 ^O	0.53 ^S	Basic
BCl ₃ /HAP	0.22 ^{Cl}	0.95 ^B	Basic

For the substrate, the LDOS showed only minor changes, which could be associated with the strong ionic character of the material and the negligible charge transferred between the adsorbed molecule and the substrate; nevertheless, the substrate LDOS decreased for the O states near the Fermi level, especially for SO₂ and BCl₃, which could be related to the increase in the work function, since the lower LDOS values indicate fewer electrons with an energy close to the Fermi level.

IV. INSIGHTS INTO HAP(0001) ADSORBED SYSTEMS

Experiments have shown that the characterization of Lewis acidic and Lewis basic adsorption sites on substrates should preferably involve probe molecules with dominant basic and acidic properties, respectively [63,68,69]. The practical limitation for this type of analysis is that the substrate's acidity and basicity cannot be fully assessed because the characterization can be influenced by the physicochemical properties of the selected probe molecule [68]. Based on our findings, we identified that simultaneous acid-base interactions occurred in the adsorption of all investigated molecules, which could introduce further difficulties to distinguish the HAP surface sites.

To understand which type of interaction is dominant for each probe molecule, we employed the DDEC6 approach [70] to compute the individual bond orders between the adsorbed molecule and the preferential acidic (Ca^{2+} ions) and basic (PO_4^{3-} groups) adsorption sites (Table V). From these values, we assigned whether the interaction *Mol*/HAP occurs predominantly via acidic, basic, or both regions based on the magnitude of the bond orders. For CO, CO₂, and NH₃, the population of the electrons is greater between the anionic termination of the molecule and the Ca^{2+} ion, which has Lewis acidic properties due to its ability to accept neighboring charges. Conversely, for SO₂ and BCl₃, greater values occur between the cationic termination of the molecule and the O of PO_4^{3-} , which has Lewis basic properties. For the remaining probe molecules, C₂H₂, CH₄, H₂, and H₂O, we note an adsorption at equally important acidic and basic sites,

as both substrate regions interact equally with the molecule via termination of opposing charges.

Concerning the role of vacuum-exposed Ca^{2+} ions as Lewis acidic sites, spectroscopic measurements revealed that both amorphous and crystalline HAP are similar in terms of Lewis acid strength [71]. Furthermore, previous DFT studies computed Ca^{2+} ions as the most HAP acidic sites via the adsorption of CO, where the distances from the carbon atom of CO to the HAP(0001), HAP(0010)_{Ca-rich}, and HAP(0010)_{P-rich} surfaces stayed between 2.7 and 2.8 Å [19,59]. Calorimetric and *ab initio* calculations for the adsorption of H₂O on HAP(0001) and HAP(0010) also indicated a strong interaction between adsorbate and exposed Ca^{2+} ions, followed by an additional reinforcement from the H-bond interaction with the basic oxygen atoms of neighboring PO_4^{3-} groups [58]. Although we only investigated the HAP(0001) termination, our adsorption results are consistent with previous studies, indicating that our model could also capture results seen in other HAP faces. These conclusions, however, should not be considered definitive for nonspecified HAP faces without further detailed investigation, since the properties of the same adsorption sites may differ for nonstoichiometric and defective surfaces.

As often used in characterization studies, CO and NH₃ can be considered suitable probe molecules for the direct assessment of HAP(0001) acidic sites. The main distinction between these two probe molecules is that the cationic termination of CO barely interacts with the HAP surface. Conversely, the assessment of HAP(0001) basic sites via the adsorption of CO₂ would result from an indirect measurement of acidic sites, due to the predominant interaction seen between its O atom and Ca^{2+} ions. Future studies on other surface planes and under different temperature and pressure conditions could provide details regarding the adsorption of CO₂ and its interaction with HAP basic sites. From the computed bond order values, SO₂ and BCl₃ were the only molecules that mostly interacted with HAP(0001) basic sites; as for the remaining molecules (C₂H₂, CH₄, H₂, and H₂O), the interaction with HAP(0001) was equally balanced between acidic and basic surface sites.

V. CONCLUSIONS

In the present study, we employed *ab initio* DFT calculations to characterize the adsorption of CO, CO₂, C₂H₂, CH₄, H₂, H₂O, NH₃, SO₂, and BCl₃ on the HAP(0001) surface. By evaluating the geometric, energetic, and electronic properties of the adsorption systems, we showed that the Ca^{2+} ions and neighboring O atoms of PO_4^{3-} groups could be identified, respectively, as the preferential Lewis acidic and Lewis basic adsorption sites on the HAP(0001) surface. The analysis of the adsorption energies revealed that the molecule-substrate interaction was stronger for molecules with a greater electronegativity difference between their cationic and anionic atoms. As a consequence, molecules with greater adsorption energies also showed greater geometric deformation as the molecule-substrate distance became shorter. Despite the low amount of charge transferred upon adsorption, all adsorbed systems presented polarization effects due to the reorganization of the electronic density, which also contributed to

the change in the surface dipole moment. The change in the work function was linearly determined by the change in the surface dipole moment, having the geometric deformation of the substrate as the main contribution.

To explore the acidity and basicity of the HAP(0001) active sites, we evaluated the redistribution of the electron density and the change in the atomic charges, thus confirming Lewis acidic properties for the Ca^{2+} ions and Lewis basic properties for neighboring O atoms of PO_4^{3-} groups. Moreover, this acid-base pair was identified as the preferential adsorption site for all selected probe molecules, in which the molecule-substrate interaction could be simultaneously stabilized by the positively and negatively charged terminations exposed on the surface. The computed bond orders also support the fact that the characterization of HAP(0001) active sites could be influenced by the properties of the selected probe molecule, as simultaneous acid-base interactions occur for the same adsorption site. In this respect, our results contribute to an atomistic understanding of the adsorption of probe molecules on the HAP(0001) surface, which could be useful for the appropriate selection of probe molecules to characterize the acid-base properties of HAP surfaces.

All results obtained in this work are reported in the paper. Additional analyses and the atomic coordinates of the opti-

mized lowest-energy adsorption configurations are available in the Supplemental Material. Additional data can be obtained upon request directly to the author.

ACKNOWLEDGMENTS

The authors gratefully acknowledge support from the São Paulo Research Foundation (FAPESP; Grant Nos. 2017/11631-2 and 2018/21401-7), the National Council for Scientific and Technological Development (CNPq; Grant No. 143375/2019-9), and Shell and the strategic importance of the support given by ANP (Brazil's National Oil, Natural Gas and Biofuels Agency) through the R&D levy regulation. This study was financed in part by the Coordenação de Aperfeiçoamento de Pessoal de Nível Superior—Brasil (CAPES), Finance Code 001. The authors also acknowledge the referees for all critiques and suggestions, which improved the quality of our paper substantially; the National Laboratory for Scientific Computing (LNCC/MCTI; Brazil) for providing HPC resources of the SDumont supercomputer, which contributed to the research results reported in this paper, and the Department of Information Technology, Campus São Carlos, for hosting our computer cluster.

-
- [1] M. J. Olszta, X. Cheng, S. S. Jee, R. Kumar, Y.-Y. Kim, M. J. Kaufman, E. P. Douglas, and L. B. Gower, Bone structure and formation: A new perspective, *Mater. Sci. Eng. R Rep.* **58**, 77 (2007).
 - [2] K.-Y. Kwon, E. Wang, N. Chang, and S.-W. Lee, Characterization of the dominant molecular step orientations on hydroxyapatite (100) surfaces, *Langmuir* **25**, 7205 (2009).
 - [3] H. Zhou and J. Lee, Nanoscale hydroxyapatite particles for bone tissue engineering, *Acta Biomater.* **7**, 2769 (2011).
 - [4] B. Li, L. Kan, X. Zhang, J. Li, R. Li, Q. Gui, D. Qiu, F. He, N. Ma, Y. Wang, and H. Wei, Biomimetic bone-like hydroxyapatite by mineralization on supramolecular porous fiber networks, *Langmuir* **33**, 8493 (2017).
 - [5] K. Zhang, Y. Zhou, C. Xiao, W. Zhao, H. Wu, J. Tang, Z. Li, S. Yu, X. Li, L. Min, Z. Yu, G. Wang, L. Wang, K. Zhang, X. Yang, X. Zhu, C. Tu, and X. Zhang, Application of hydroxyapatite nanoparticles in tumor-associated bone segmental defect, *Sci. Adv.* **5**, eaax6946 (2019).
 - [6] O. Geuli, N. Metoki, T. Zada, M. Reches, N. Eliaz, and D. Mandler, Synthesis, coating, and drug-release of hydroxyapatite nanoparticles loaded with antibiotics, *J. Mater. Chem. B* **5**, 7819 (2017).
 - [7] M. L. Martins, T. S. Pinto, A. M. Gomes, J. P. R. L. L. Parra, G. C. Franchi, W. F. Zambuzzi, and C. G. Rodrigues, Immobilization of paclitaxel on hydroxyapatite for breast cancer investigations, *Langmuir* **36**, 8723 (2020).
 - [8] C. M. Curtin, G. M. Cunniffe, F. G. Lyons, K. Bessho, G. R. Dickson, G. P. Duffy, and F. J. O'Brien, Innovative collagen nano-hydroxyapatite scaffolds offer a highly efficient non-viral gene delivery platform for stem cell-mediated bone formation, *Adv. Mater.* **24**, 749 (2012).
 - [9] K. Deshmukh, M. M. Shaik, S. R. Ramanan, and M. Kowshik, Self-activated fluorescent hydroxyapatite nanoparticles: A promising agent for bioimaging and biolabeling, *ACS Biomater. Sci. Eng.* **2**, 1257 (2016).
 - [10] A. Fihri, C. Len, R. S. Varma, and A. Solhy, Hydroxyapatite: A review of syntheses, structure and applications in heterogeneous catalysis, *Coord. Chem. Rev.* **347**, 48 (2017).
 - [11] M. Miyauchi, T. Watanabe, D. Hoshi, and T. Ohba, Irreversible adsorption of acidic, basic, and water gas molecules on calcium-deficient hydroxyapatite, *Dalton Trans.* **48**, 17507 (2019).
 - [12] S. Diallo-Garcia, M. B. Osman, J.-M. Krafft, S. Casale, C. Thomas, J. Kubo, and G. Costentin, Identification of surface basic sites and acid-base pairs of hydroxyapatite, *J. Phys. Chem. C* **118**, 12744 (2014).
 - [13] S. Diallo-Garcia, M. B. Osman, J.-M. Krafft, S. Boujday, and C. Guylène, Discrimination of infrared fingerprints of bulk and surface POH and OH of hydroxyapatites, *Catal. Today* **226**, 81 (2014).
 - [14] M. B. Osman, S. D. Garcia, J.-M. Krafft, C. Methivier, J. Blanchard, T. Yoshioka, J. Kubo, and G. Costentin, Control of calcium accessibility over hydroxyapatite by post-precipitation steps: Influence on the catalytic reactivity toward alcohols, *Phys. Chem. Chem. Phys.* **18**, 27837 (2016).
 - [15] J. Moulijn, P. van Leeuwen, and R. van Santen, Catalyst characterization with spectroscopic techniques, in *Catalysis—An Integrated Approach to Homogeneous, Heterogeneous and Industrial Catalysis* (Elsevier, Amsterdam, 1993), pp. 363–400.

- [16] A. Slepko and A. A. Demkov, First principles study of hydroxyapatite surface, *J. Chem. Phys.* **139**, 044714 (2013).
- [17] M. Corno, A. Rimola, V. Bolis, and P. Ugliengo, Hydroxyapatite as a key biomaterial: Quantum-mechanical simulation of its surfaces in interaction with biomolecules, *Phys. Chem. Chem. Phys.* **12**, 6309 (2010).
- [18] A. Slepko and A. A. Demkov, First-principles study of the biomineral hydroxyapatite, *Phys. Rev. B* **84**, 134108 (2011).
- [19] F. Chiatti, M. Corno, Y. Sakhno, G. Martra, and P. Ugliengo, Revealing hydroxyapatite nanoparticle surface structure by CO adsorption: A combined B3LYP and infrared study, *J. Phys. Chem. C* **117**, 25526 (2013).
- [20] S. Hu, F. Jia, C. Marinescu, F. Cimpoesu, Y. Qi, Y. Tao, A. Stroppa, and W. Ren, Ferroelectric polarization of hydroxyapatite from density functional theory, *RSC Adv.* **7**, 21375 (2017).
- [21] M. Corno, R. Orlando, B. Civalleri, and P. Ugliengo, Periodic B3LYP study of hydroxyapatite (001) surface modelled by thin layer slabs, *Eur. J. Mineral.* **19**, 757 (2007).
- [22] K. Kandori, T. Kuroda, S. Togashi, and E. Katayama, Preparation of calcium hydroxyapatite nanoparticles using microreactor and their characteristics of protein adsorption, *J. Phys. Chem. B* **115**, 653 (2011).
- [23] T. Tsuchida, J. Kubo, T. Yoshioka, S. Sakuma, T. Takeguchi, and W. Ueda, Reaction of ethanol over hydroxyapatite affected by Ca/P ratio of catalyst, *J. Catal.* **259**, 183 (2008).
- [24] S. Ogo, A. Onda, Y. Iwasa, K. Hara, A. Fukuoka, and K. Yanagisawa, 1-Butanol synthesis from ethanol over strontium phosphate hydroxyapatite catalysts with various Sr/P ratios, *J. Catal.* **296**, 24 (2012).
- [25] P. Hohenberg and W. Kohn, Inhomogeneous electron gas, *Phys. Rev.* **136**, B864 (1964).
- [26] W. Kohn and L. J. Sham, Self-consistent equations including exchange and correlation effects, *Phys. Rev.* **140**, A1133 (1965).
- [27] J. P. Perdew, K. Burke, and M. Ernzerhof, Generalized Gradient Approximation Made Simple, *Phys. Rev. Lett.* **77**, 3865 (1996).
- [28] S. Grimme, J. Antony, S. Ehrlich, and H. Krieg, A consistent and accurate *ab initio* parametrization of density functional dispersion correction (DFT-d) for the 94 elements H-Pu, *J. Chem. Phys.* **132**, 154104 (2010).
- [29] G. Kresse and J. Hafner, *Ab initio* molecular dynamics for open-shell transition metals, *Phys. Rev. B* **48**, 13115 (1993).
- [30] G. Kresse and J. Furthmüller, Efficient iterative schemes for *ab initio* total-energy calculations using a plane-wave basis set, *Phys. Rev. B* **54**, 11169 (1996).
- [31] G. Kresse and D. Joubert, From ultrasoft pseudopotentials to the projector augmented-wave method, *Phys. Rev. B* **59**, 1758 (1999).
- [32] H. Gollisch and L. Fritsche, Relativistic one-particle equation for electron states of heavy metals, *Phys. Status Solidi B* **86**, 145 (1978).
- [33] T. Takeda, The scalar relativistic approximation, *Z. Phys. B* **32**, 43 (1978).
- [34] See Supplemental Material at <http://link.aps.org/supplemental/10.1103/PhysRevMaterials.5.075003> for additional analyses and optimized atomic coordinates, which includes Refs. [18,27,28,36–39,42–45,49,51–54,66,72–79].
- [35] H. J. Monkhorst and J. D. Pack, Special points for Brillouin-zone integrations, *Phys. Rev. B* **13**, 5188 (1976).
- [36] R. D. Johnson, NIST computational chemistry comparison and benchmark database, NIST Standard Reference Database Number 101 Release 21 (National Institute of Standards and Technology, Gaithersburg, 2020).
- [37] J. M. Hughes, M. Cameron, and K. D. Crowley, Structural variations in natural F, OH, and Cl apatites, *Am. Mineral.* **74**, 870 (1989).
- [38] D. Haverty, S. A. M. Tofail, K. T. Stanton, and J. B. McMonagle, Structure and stability of hydroxyapatite: Density functional calculation and rietveld analysis, *Phys. Rev. B* **71**, 094103 (2005).
- [39] M. Corno, C. Busco, B. Civalleri, and P. Ugliengo, Periodic *ab initio* study of structural and vibrational features of hexagonal hydroxyapatite $\text{Ca}_{10}(\text{PO}_4)_6(\text{OH})_2$, *Phys. Chem. Chem. Phys.* **8**, 2464 (2006).
- [40] N. Almora-Barrios, K. F. Austen, and N. H. de Leeuw, Density functional theory study of the binding of glycine, proline, and hydroxyproline to the hydroxyapatite (0001) and (01 $\bar{1}$ 0) surfaces, *Langmuir* **25**, 5018 (2009).
- [41] M. B. Osman, J.-M. Krafft, C. Thomas, T. Yoshioka, J. Kubo, and G. Costentin, Importance of the nature of the active acid/base pairs of hydroxyapatite involved in the catalytic transformation of ethanol to *n*-butanol revealed by *operando* DRIFTS, *ChemCatChem* **11**, 1765 (2019).
- [42] C. Alcock, Gaseous reaction kinetics and molecular decomposition, in *Thermochemical Processes* (Elsevier, Amsterdam, 2001), pp. 42–85.
- [43] B. Ruscic, Active thermochemical tables: Sequential bond dissociation enthalpies of methane, ethane, and methanol and the related thermochemistry, *J. Phys. Chem. A* **119**, 7810 (2015).
- [44] W. Haynes, *CRC Handbook of Chemistry and Physics*, 97th ed. (CRC Press, Boca Raton, FL, 2016).
- [45] T. A. Manz and N. G. Limas, Introducing DDEC6 atomic population analysis: Part 1. Charge partitioning theory and methodology, *RSC Adv.* **6**, 47771 (2016).
- [46] N. G. Limas and T. A. Manz, Introducing DDEC6 atomic population analysis: Part 2. Computed results for a wide range of periodic and nonperiodic materials, *RSC Adv.* **6**, 45727 (2016).
- [47] G. Frenking, C. Loschen, A. Krapp, S. Fau, and S. H. Strauss, Electronic structure of CO—An exercise in modern chemical bonding theory, *J. Comput. Chem.* **28**, 117 (2007).
- [48] A. L. Hickey and C. N. Rowley, Benchmarking quantum chemical methods for the calculation of molecular dipole moments and polarizabilities, *J. Phys. Chem. A* **118**, 3678 (2014).
- [49] J. C. Elliott, P. E. Mackie, and R. A. Young, Monoclinic hydroxyapatite, *Science* **180**, 1055 (1973).
- [50] A. T. Sanger and W. F. Kuhs, Structural disorder in hydroxyapatite, *Z. Kristallogr. Cryst. Mater.* **199**, 123 (1992).
- [51] F. Chiatti, M. Corno, and P. Ugliengo, Stability of the dipolar (001) surface of hydroxyapatite, *J. Phys. Chem. C* **116**, 6108 (2012).
- [52] L. A. Avakyan, E. V. Paramonova, J. Coutinho, S. oberg, V. S. Bystrov, and L. A. Bugaev, Optoelectronics and defect levels in hydroxyapatite by first-principles, *J. Chem. Phys.* **148**, 154706 (2018).

- [53] S. Kasamatsu and O. Sugino, First-principles investigation of polarization and ion conduction mechanisms in hydroxyapatite, *Phys. Chem. Chem. Phys.* **20**, 8744 (2018).
- [54] G. Ulian and G. Valdrè, Second-order elastic constants of hexagonal hydroxylapatite (P6₃) from *ab initio* quantum mechanics: Comparison between DFT functionals and basis sets, *Int. J. Quantum Chem.* **118**, e25500 (2018).
- [55] A. Haider, S. Haider, S. S. Han, and I.-K. Kang, Recent advances in the synthesis, functionalization and biomedical applications of hydroxyapatite: A review, *RSC Adv.* **7**, 7442 (2017).
- [56] G. Ma and X. Y. Liu, Hydroxyapatite: Hexagonal or monoclinic?, *Cryst. Growth Des.* **9**, 2991 (2009).
- [57] S. Nakamura, H. Takeda, and K. Yamashita, Proton transport polarization and depolarization of hydroxyapatite ceramics, *J. Appl. Phys.* **89**, 5386 (2001).
- [58] M. Corno, C. Busco, V. Bolis, S. Tosoni, and P. Ugliengo, Water adsorption on the stoichiometric (001) and (010) surfaces of hydroxyapatite: A periodic B3LYP study, *Langmuir* **25**, 2188 (2009).
- [59] V. Bolis, C. Busco, G. Martra, L. Bertinetti, Y. Sakhno, P. Ugliengo, F. Chiatti, M. Corno, and N. Roveri, Coordination chemistry of Ca sites at the surface of nanosized hydroxyapatite: Interaction with H₂O and CO, *Philos. Trans. R. Soc. A* **370**, 1313 (2012).
- [60] P. Rulis, H. Yao, L. Ouyang, and W. Y. Ching, Electronic structure, bonding, charge distribution, and x-ray absorption spectra of the (001) surfaces of fluorapatite and hydroxyapatite from first principles, *Phys. Rev. B* **76**, 245410 (2007).
- [61] L. Mino, A. M. Ferrari, V. Lacivita, G. Spoto, S. Bordiga, and A. Zecchina, CO adsorption on anatase nanocrystals: A combined experimental and periodic DFT study, *J. Phys. Chem. C* **115**, 7694 (2011).
- [62] P. C. D. Mendes, V. K. Ocampo-Restrepo, and J. L. F. Da Silva, Ab initio investigation of quantum size effects on the adsorption of CO₂, CO, H₂O, and H₂ on transition-metal particles, *Phys. Chem. Chem. Phys.* **22**, 8998 (2020).
- [63] K. I. Hadjiivanov and G. N. Vayssilov, Characterization of oxide surfaces and zeolites by carbon monoxide as an IR probe molecule, in *Advances in Catalysis, Vol. 47* (Elsevier, Amsterdam, 2002), pp. 307–511.
- [64] A. D. Walsh, 470. The electronic orbitals, shapes, and spectra of polyatomic molecules. Part V. Tetratomic, non-hydride molecules, AB₃, *J. Chem. Soc.*, 2301 (1953), doi: 10.1039/JR9530002301.
- [65] A. D. Walsh, 467. The electronic orbitals, shapes, and spectra of polyatomic molecules. Part II. Non-hydride AB₂ and BAC molecules, *J. Chem. Soc.*, 2266 (1953), doi: 10.1039/JR9530002266.
- [66] T. C. Leung, C. L. Kao, W. S. Su, Y. J. Feng, and C. T. Chan, Relationship between surface dipole, work function and charge transfer: Some exceptions to an established rule, *Phys. Rev. B* **68**, 195408 (2003).
- [67] W.-X. Li, C. Stampfl, and M. Scheffler, Oxygen adsorption on Ag(111): A density-functional theory investigation, *Phys. Rev. B* **65**, 075407 (2002).
- [68] J. A. Lercher, C. Gründling, and G. Eder-Mirth, Infrared studies of the surface acidity of oxides and zeolites using adsorbed probe molecules, *Catal. Today* **27**, 353 (1996).
- [69] J. Lavalley, Infrared spectrometric studies of the surface basicity of metal oxides and zeolites using adsorbed probe molecules, *Catal. Today* **27**, 377 (1996).
- [70] T. A. Manz, Introducing DDEC6 atomic population analysis: Part 3. Comprehensive method to compute bond orders, *RSC Adv.* **7**, 45552 (2017).
- [71] Y. Sakhno, L. Bertinetti, M. Iafisco, A. Tampieri, N. Roveri, and G. Martra, Surface hydration and cationic sites of nanohydroxyapatites with amorphous or crystalline surfaces: A comparative study, *J. Phys. Chem. C* **114**, 16640 (2010).
- [72] S. Grimme, Semiempirical GGA-type density functional constructed with a long-range dispersion correction, *J. Comput. Chem.* **27**, 1787 (2006).
- [73] J. P. Perdew, A. Ruzsinszky, G. I. Csonka, O. A. Vydrov, G. E. Scuseria, L. A. Constantin, X. Zhou, and K. Burke, Restoring the Density-Gradient Expansion for Exchange in Solids and Surfaces, *Phys. Rev. Lett.* **100**, 136406 (2008).
- [74] K. Matsunaga, Theoretical investigation of the defect formation mechanism relevant to nonstoichiometry in hydroxyapatite, *Phys. Rev. B* **77**, 104106 (2008).
- [75] N. T. T. Linh, P. D. Tuan, and N. V. Dzung, The shifts of band gap and binding energies of titania/hydroxyapatite material, *J. Compos.* **2014**, 1 (2014).
- [76] F. J. Cruz, M. E. M. da Piedade, and J. C. Calado, Standard molar enthalpies of formation of hydroxy-, chlor-, and bromapatite, *J. Chem. Thermodyn.* **37**, 1061 (2005).
- [77] G. Ulian, D. Moro, and G. Valdrè, First-principles study of structural and surface properties of (001) and (010) surfaces of hydroxylapatite and carbonated hydroxylapatite, *J. Appl. Crystallogr.* **49**, 1893 (2016).
- [78] M. Ernzerhof and G. E. Scuseria, Assessment of the Perdew–Burke–Ernzerhof exchange-correlation functional, *J. Chem. Phys.* **110**, 5029 (1999).
- [79] H. Solheim, K. Ruud, and P.-O. Åstrand, Atomic dipole moments calculated using analytical molecular second-moment gradients, *J. Chem. Phys.* **120**, 10368 (2004).